Supplementary Material

Broadband gate-reconfigurable infrared sensing based on a b-$As_{0.3}P_{0.7}$/MoS_2 heterojunction

Yuelin Zhang[1], Tangxin Li[2], Yuxuan Pei[3], Ziyue Song[4], Hangyu Xu[2], Xiao Fu[2], Mingkai Li[1, †] and Min Luo[2, †]

[1]Hubei University, Wuhan 430062, China
[2]Shanghai Institute of Technical Physics, Chinese Academy of Sciences, Shanghai 200083, China
[3]Beihang University, Beijing 100191, China
[4]Wuhan University, Wuhan 430072, China

*Correspondence should be addressed to
Min Luo: luomin17@mails.ucas.ac.cn
Mingkai Li: mkli@hubu.edu.cn

Section 1: Photodetection Performance Metrics

The wavelength-dependent responsivity, noise-equivalent power, and input-referred specific detectivity were calculated from the dark-current-subtracted photocurrent, incident optical power, effective detector area, and experimentally measured current-noise spectral density. The photocurrent was determined as

$$I_{ph} = |I_{light} - I_{dark}| \quad (1)$$

where I_{light} and I_{dark} are the currents measured under illuminated and dark conditions, respectively. At zero drain bias, the dark-current-subtracted photocurrent corresponds to the magnitude of the short-circuit current.

The responsivity (R) was calculated using

$$R = \frac{I_{ph}}{P_{in}} \quad (2)$$

where P_{in} is the optical power incident on the illuminated detector region.

The effective detector area was taken as the b-$As_{0.3}P_{0.7}$/MoS_2 overlap region. Approximating this region as a circle with a diameter of 30 μm gives

$$A_{device} = \pi(r)^2 \quad (3)$$

where A_{device} is the effective active area of the b-$As_{0.3}P_{0.7}$/MoS_2 heterojunction, π is the mathematical constant, and r is the effective radius of the active detector region.

The noise-equivalent power was calculated as

$$NEP = \frac{i_n}{R} \quad (4)$$

and the input-referred specific detectivity was estimated from

$$D^* = \frac{\sqrt{A_{device}}}{NEP} = \frac{R\sqrt{A_{device}}}{i_n} \quad (5)$$

Because i_n is expressed as a current-noise amplitude spectral density in $\mathrm{A\,Hz^{-1/2}}$, no additional bandwidth factor is required in this expression. The unit of D^* is $\mathrm{cm\,Hz^{1/2}W^{-1}}$, conventionally expressed as Jones.

The effective photosensitive area was estimated from the b-$As_{0.3}P_{0.7}$/MoS_2 overlap region:

$$A_{device} = 706.86\ \mu\mathrm{m}^2 = 7.07 \times 10^{-6}\ \mathrm{cm}^2$$

and therefore

$$\sqrt{A_{device}} = 2.66 \times 10^{-3}\ \mathrm{cm}$$

The representative input-referred current-noise spectral density extracted from the white-noise plateau over the 1-10 kHz frequency range was

$$i_n = 5.61 \times 10^{-16}\ \mathrm{A\,Hz^{-1/2}}$$

Under 1550 nm illumination at $V_{ds} = 0$ V and $V_g = 0$ V, the dark-current-subtracted short-circuit current was

$$I_{ph,1550} = 5.867 \times 10^{-7}\ \mathrm{A}$$

The effective optical power incident on the detector was

$$P_{in,1550} = 3.20 \times 10^{-6}\ \mathrm{W}.$$

The zero-bias responsivity was therefore

$$R_{1550} = \frac{5.867 \times 10^{-7}\ \mathrm{A}}{3.20 \times 10^{-6}\ \mathrm{W}} = 0.1833\ \mathrm{A\,W^{-1}} \approx 0.183\ \mathrm{A\,W^{-1}}.$$

The corresponding noise-equivalent power was

$$NEP_{1550} = \frac{5.61 \times 10^{-16}\mathrm{A\,Hz^{-1/2}}}{0.1833\ \mathrm{A\,W^{-1}}} = 3.06 \times 10^{-15}\ \mathrm{W\,Hz^{-1/2}}.$$

Using the effective junction area defined above, the input-referred specific detectivity was

$$D^*_{1550} = \frac{(0.1833\ \mathrm{A\,W^{-1}})(2.6587 \times 10^{-3}\ \mathrm{cm})}{5.61 \times 10^{-16}\ \mathrm{A\,Hz^{-1/2}}} = 8.69 \times 10^{11}\ \mathrm{Jones}.$$

Therefore, the 1550 nm zero-bias responsivity and input-referred specific detectivity are approximately 0.183 A W^{-1} and 8.69×10^{11} Jones, respectively.

The 4050 nm measurement was performed at $V_{ds} = 0$ V and $V_g = 0$ V. The incident optical power density was

$$p_{4050} = 2.2 \times 10^{5}\ \mathrm{mW\,cm^{-2}} = 220\ \mathrm{W\,cm^{-2}}.$$

The measured laser-spot diameter was 13.35 μm, corresponding to a spot radius of

$$r_{spot} = \frac{13.35\ \mu\mathrm{m}}{2} = 6.675\ \mu\mathrm{m}.$$

The illuminated spot area was therefore

$$A_{spot} = \pi r_{spot}^2 = \pi(6.675\ \mu\mathrm{m})^2 = 139.97\ \mu\mathrm{m}^2.$$

After conversion to square centimetres,

$$A_{spot} = 139.97 \times 10^{-8}\ \mathrm{cm}^2 = 1.40 \times 10^{-6}\ \mathrm{cm}^2.$$

The 13.35 μm laser spot was smaller than the approximately 30 μm active-junction diameter and was positioned within the b-$As_{0.3}P_{0.7}$/MoS_2 overlap region. Therefore, the optical power incident on the device was calculated using the illuminated spot area:

$$P_{in,4050} = p_{4050}A_{spot} = (220\ \mathrm{W\,cm^{-2}})(1.3997 \times 10^{-6}\ \mathrm{cm}^2) = 3.08 \times 10^{-4}\ \mathrm{W}$$
$$= 0.308\ \mathrm{mW}.$$

The measured dark-current-subtracted photocurrent was approximately

$$I_{ph,4050} = 1.76 \times 10^{-6}\ \mathrm{A}.$$

The corresponding zero-bias responsivity was

$$R_{4050} = \frac{1.76 \times 10^{-6}\ \mathrm{A}}{3.08 \times 10^{-4}\ \mathrm{W}} \approx 5.7 \times 10^{-3}\ \mathrm{A\,W^{-1}}.$$

The noise-equivalent power was then calculated as

$$NEP_{4050} = \frac{5.61 \times 10^{-16}\ \mathrm{A\,Hz^{-1/2}}}{5.7 \times 10^{-3}\ \mathrm{A\,W^{-1}}} = 9.84 \times 10^{-14}\ \mathrm{W\,Hz^{-1/2}}.$$

For the specific-detectivity calculation, the active b-$As_{0.3}P_{0.7}/MoS_2$ junction area was used rather than the laser-spot area. Accordingly,

$$D^*_{4050} = \frac{(5.7 \times 10^{-3}\ \mathrm{A\,W^{-1}})(2.6587 \times 10^{-3}\ \mathrm{cm})}{5.61 \times 10^{-16}\ \mathrm{A\,Hz^{-1/2}}} = 2.70 \times 10^{10}\ \mathrm{Jones}.$$

Therefore, the 4050 nm zero-bias responsivity and input-referred specific detectivity are approximately 5.7×10^{-3} A W^{-1} and 2.70×10^{10} Jones, respectively.

The calculated D^* values are input-referred estimates based on the 1-10 kHz white-noise plateau, which approaches the measurement-system background; they should not be interpreted as low-frequency, fully de-embedded intrinsic detectivities.

Estimated optical conditions. The calculation below assumes a total 520 nm optical power of approximately 2.00 mW and a laser-spot radius of approximately 150 μm (spot diameter: 300 μm). These estimated values should be replaced with calibrated sample-plane measurements before publication. The optical power is assumed to be uniformly distributed over the laser spot, and the spot is assumed to be centred on the active heterojunction.

Under 520 nm illumination at $V_{\mathrm{ds}} = 0$ V and $V_{\mathrm{g}} = 0$ V, the measured illuminated and dark currents were

$$I_{light} =- 1.0266 \times 10^{-7}\ \mathrm{A}$$

and

$$I_{dark} =- 2.0 \times 10^{-14}\ \mathrm{A},$$

respectively. The dark-current-subtracted short-circuit photocurrent was therefore

$$I_{ph,520} = |\mathrm{I_{light}} - \mathrm{I_{dark}}|$$

$$= |-1.0266 \times 10^{-7} - (-2.0 \times 10^{-14})| \approx 1.0266 \times 10^{-7}\ \mathrm{A}.$$

The adopted total optical power and laser-spot radius were

$$P_{total} = 2.00 \times 10^{-3}\ \mathrm{W}$$

and

$$r_{spot} = 150\ \mu\mathrm{m} = 1.50 \times 10^{-2}\ \mathrm{cm},$$

respectively. The laser-spot area was therefore

$$A_{spot} = \pi r_{spot}^2 = \pi(150\ \mu\mathrm{m})^2 = 7.0686 \times 10^4\ \mu\mathrm{m}^2 = 7.0686 \times 10^{-4}\ \mathrm{cm}^2.$$

The corresponding average optical power density was

$$p_{520} = \frac{P_{total}}{A_{spot}} = \frac{2.00 \times 10^{-3}}{7.0686 \times 10^{-4}} = 2.829\ \mathrm{W\,cm^{-2}} = 2.829 \times 10^{3}\ \mathrm{mW\,cm^{-2}}.$$

The active b-$As_{0.3}P_{0.7}/MoS_2$ heterojunction was approximated as a circular region with a diameter of 30 μm. Its effective area was

$$A_{device} = \pi\left(\frac{30\ \mu m}{2}\right)^2 = 706.86\ \mu\text{m}^2 = 7.0686 \times 10^{-6}\ \text{cm}^2.$$

Because the 300 μm laser-spot diameter was larger than the approximately 30 μm active-junction diameter, only the geometrical fraction of the total optical power incident on the active junction was used. The effective incident power was

$$P_{in,520} = P_{total}\frac{A_{device}}{A_{spot}}$$

$$= (2.00 \times 10^{-3}\ \text{W})\frac{7.0686 \times 10^{-6}}{7.0686 \times 10^{-4}} = 2.00 \times 10^{-5}\ \text{W} = 20.0\ \mu\text{W}.$$

The zero-bias responsivity was calculated as

$$R_{520} = \frac{I_{ph,520}}{P_{in,520}} = \frac{1.0266 \times 10^{-7}}{2.00 \times 10^{-5}} = 5.133 \times 10^{-3}\ \text{A W}^{-1} = 5.133\ \text{mA W}^{-1}.$$

Using the representative input-referred current-noise spectral density of $i_n = 5.61 \times 10^{-16}\ \text{A Hz}^{-1/2}$, the noise-equivalent power was

$$NEP_{520} = \frac{i_n}{R_{520}} = \frac{5.61 \times 10^{-16}}{5.133 \times 10^{-3}} = 1.09 \times 10^{-13}\ \text{W Hz}^{-1/2}.$$

The square root of the effective detector area was

$$\sqrt{A_{device}} = 2.6587 \times 10^{-3}\ \text{cm}.$$

The input-referred specific detectivity was then calculated as

$$D^*_{520} = \frac{R_{520}\sqrt{A_{device}}}{i_n}$$

$$= \frac{(5.133 \times 10^{-3})(2.6587 \times 10^{-3})}{5.61 \times 10^{-16}} = 2.43 \times 10^{10}\ \text{Jones}.$$

Therefore, under the adopted estimated optical conditions, the 520 nm zero-bias responsivity, noise-equivalent power, and input-referred specific detectivity are approximately $5.13\ \text{mA W}^{-1}$, $1.09 \times 10^{-13}\ \text{W Hz}^{-1/2}$, and 2.43×10^{10} Jones, respectively. Because the adopted noise floor approaches the measurement-system background, the reported D^* value is regarded as an input-referred estimate rather than a fully de-embedded intrinsic detectivity.

Section 2: Supplementary Figures

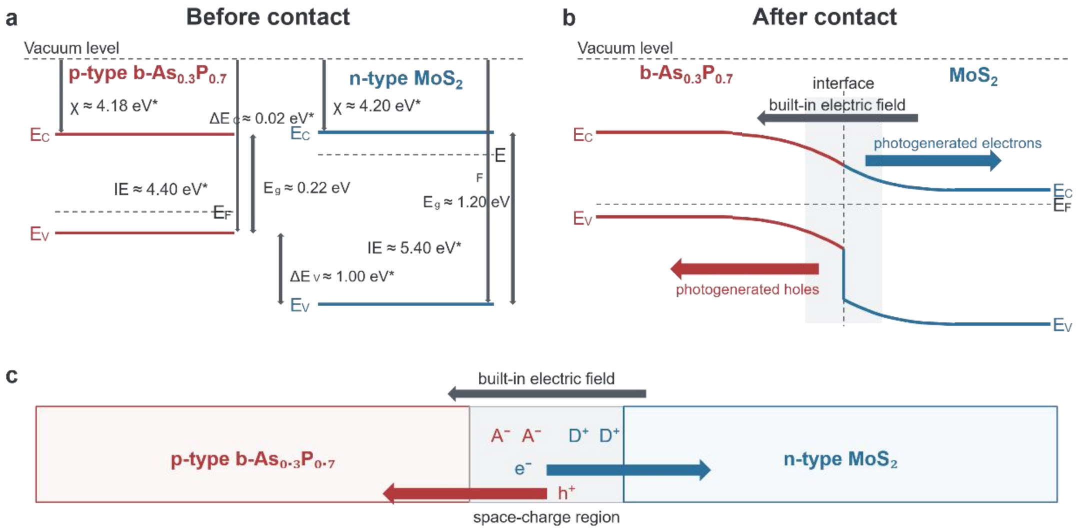

Figure S1. Literature-supported schematic band alignment and carrier-separation mechanism of the b-As$_{0.3}$P$_{0.7}$/MoS$_2$ heterojunction. (a) Isolated p-type b-As$_{0.3}$P$_{0.7}$ and n-type multilayer MoS$_2$ before contact. The representative literature-guided values are $E_g \approx 0.22$ eV, $\chi \approx 4.18$ eV, and IE $\approx$ 4.40 eV for b-As$_{0.3}$P$_{0.7}$; and $E_g \approx 1.20$ eV, $\chi \approx 4.20$ eV, and $IE \approx 5.40$ eV for MoS$_2$. The corresponding electron-affinity-rule estimates are $\Delta E_C \approx 0.02$ eV and $\Delta E_V \approx 1.00$ eV. (b) Fermi-level equilibration and interfacial band bending after contact. (c) Built-in electric field and photocarrier-separation directions. The values are schematic estimates based on Refs. 8-14 and 21 of the main text; because ultraviolet photoelectron spectroscopy and Kelvin-probe measurements were not performed on the present device, no experimentally determined quantitative band offsets are claimed.

Figure S1 presents the literature-guided band alignment of the b-As$_{0.3}$P$_{0.7}$/MoS$_2$ heterojunction before and after contact. The bandgaps of multilayer b-As$_{0.3}$P$_{0.7}$ and MoS$_2$ are approximately 0.22 and 1.2 eV[1, 2], respectively. Based on the reported electron affinity of MoS$_2$and the previously reported MoS$_2$/AsP valence-band offset, the approximate electron affinities of b-As$_{0.3}$P$_{0.7}$ and MoS$_2$ are 4.18 and 4.00 eV[3], respectively, and the corresponding conduction- and valence-band offsets are approximately 0.18 and 0.80 eV[4], respectively. These literature-derived values are used only to construct a schematic band diagram and are not regarded as directly measured parameters of the present device.

Before contact, the Fermi levels of p-type b-As$_{0.3}$P$_{0.7}$ and n-type MoS$_2$ are located close to their valence- and conduction-band edges, respectively. After contact and Fermi-level equilibration, interfacial band bending and a built-in electric field are established, facilitating the spatial separation of photogenerated electrons and holes. Under positive gate bias, MoS$_2$ is maintained in an electron-accumulated state, and further electron accumulation has only a limited effect on carrier separation. Under negative gate bias, electron depletion in MoS$_2$ weakens the interfacial potential difference and suppresses photogenerated-carrier separation, consistent with the experimentally observed reductions in I_{sc} and V_{oc}.

Here, E_g, χ, IE, ΔE_C, and ΔE_V represent the bandgap, electron affinity, ionization energy, conduction-band offset, and valence-band offset, respectively.

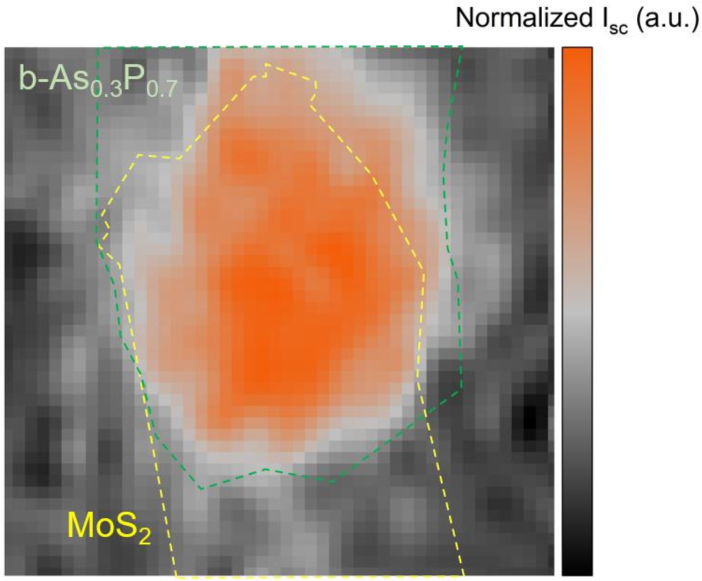

Figure S2. Scanning photocurrent microscopy map of the b-$As_{0.3}P_{0.7}$/MoS_2 heterojunction under 4050 nm illumination. The photocurrent is primarily localized in the b-$As_{0.3}P_{0.7}$/MoS_2 overlap region, supporting the contribution of the heterointerface to mid-infrared photocarrier separation and collection. Scale bar: 25 μm.

To further verify the origin of the mid-infrared photoresponse, scanning photocurrent mapping was performed under 4050 nm laser illumination. As shown in Fig. S2, the photocurrent is predominantly localized in the b-$As_{0.3}P_{0.7}$/MoS_2 overlap region, whereas the signals from the individual material regions and near the metal contacts are comparatively weak. This spatial distribution indicates that the 4050 nm photocurrent mainly originates from the b-$As_{0.3}P_{0.7}$/MoS_2 heterojunction rather than from the isolated materials or metal/semiconductor contacts. Together with the time-resolved response in Fig. 3, this result further confirms the mid-infrared detection capability of the heterojunction device.

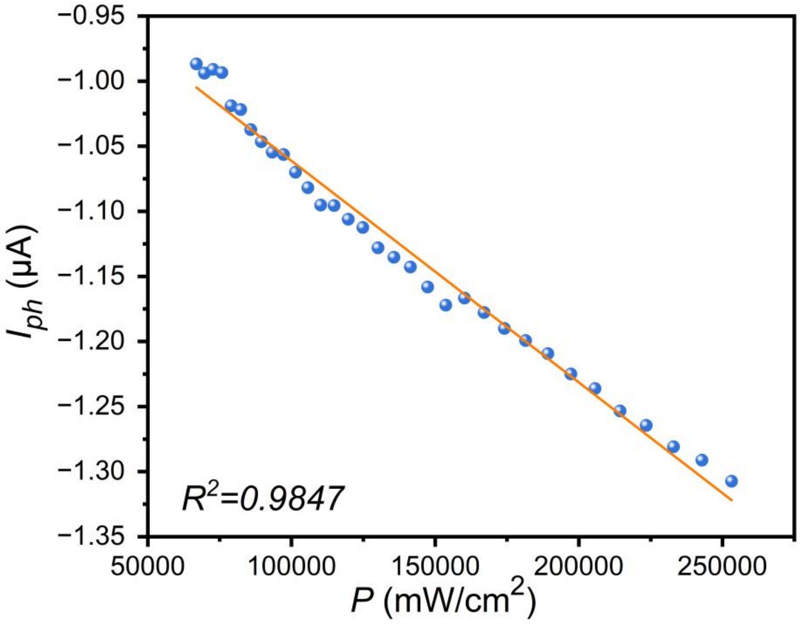

Figure S3. Power-dependent photoresponse of the b-$As_{0.3}P_{0.7}$/MoS_2 heterojunction under 4050 nm illumination. The symbols represent the experimental data, and the solid line represents a linear fit with a coefficient of determination of R^2 = 0.9847, confirming an approximately linear photoresponse over the experimentally investigated power range.

The power-dependent short-circuit photocurrent under 4050 nm illumination is shown in Fig. S3. After subtraction of the dark current, the photocurrent increases approximately linearly with incident optical power over the measured range, with R^2 = 0.9847. This linear input-output relationship provides the basis for representing optical multiplication in multiply-accumulate operations, without invoking photoconductive gain.

At 4050 nm, the responsivity and input-referred specific detectivity are estimated to be approximately 5.7×10^{-3} A W^{-1} and 2.70×10^{10} Jones, respectively. The responsivity represents a conservative estimate because the total incident beam power was used without correcting for the fraction of the optical spot outside the heterojunction region. Moreover, because the high-frequency noise approaches the measurement-system background, the specific detectivity is reported as an input-referred estimate under the present measurement configuration rather than a fully de-embedded intrinsic device value.

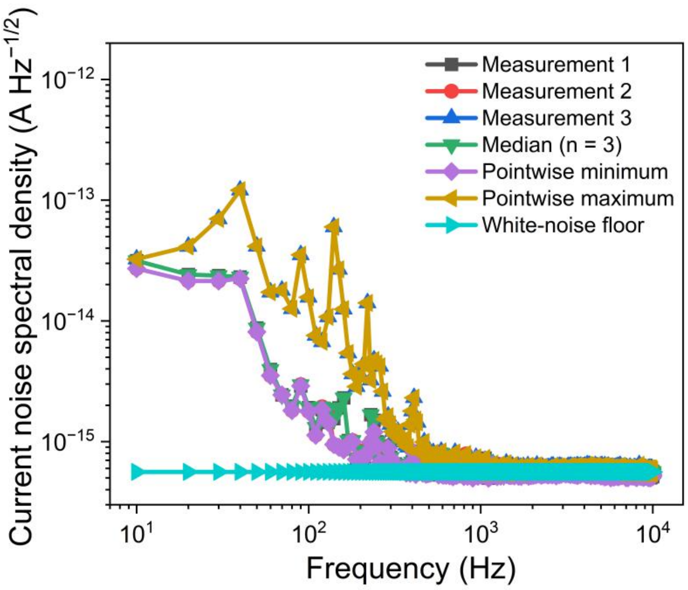

Figure S4. Input-referred current-noise spectral density of the device measured over the frequency range of 10 Hz-10 kHz. Measurements 1-3 represent three independent noise measurements. The median spectrum was calculated pointwise from the three processed measurements, while the pointwise minimum and maximum values indicate the measurement range. Pronounced peaks near 50 Hz and its harmonics originate mainly from power-line and environmental interference. The white-noise floor extracted from the nearly frequency-independent 1-10 kHz region is approximately 5.61×10^{-16} AHz$^{-1/2}$.

To further evaluate the influence of electrical noise on the distinguishability of the programmed photoresponse states, three independent current-noise measurements were performed over the frequency range of 10 Hz-10 kHz. After conversion to the input-referred current-noise spectral density and suppression of the narrowband 50 Hz power-line interference, the processed spectra reach a nearly frequency-independent white-noise plateau above approximately 1 kHz. The representative input-referred current-noise spectral density extracted from the 1-10 kHz range is approximately

$$5.61\times10^{-16} \text{ A Hz}^{-1/2}.$$

The small variation among the three measurements indicates good measurement repeatability. The relatively low and stable noise floor, together with the reproducible photocurrent states, non-overlapping error ranges, and clear differences between adjacent states, indicates that electrical noise is unlikely to prevent discrimination of the fifteen gate-programmed photoresponse states under the present measurement conditions.

Because the high-frequency noise plateau approaches the background level of the measurement system, the reported spectrum is conservatively described as the input-referred noise of the complete measurement configuration rather than a fully de-embedded intrinsic detector-noise spectrum.

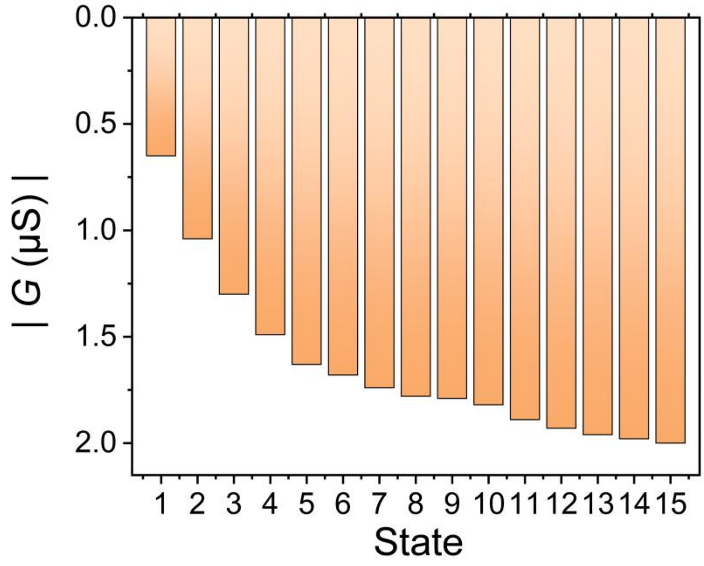

Fig. S5 Experimentally derived 15 conductance states used for G15 discretization of the classifier parameters. The electrical currents were measured at a fixed drain-source voltage of V_{ds} = 1 V, and their magnitudes were converted into conductance states using $|G_k| = |I_k|/|V_{ds}|$. The resulting conductance magnitudes range from 0.65 to 2.00 μS and were used as the experimentally accessible levels for discretizing the magnitudes of the network weights and biases.

To provide an experimental basis for the G15 constraint used in Scheme D, 15 electrical current states were measured at a fixed drain-source voltage of V_{ds} = 1 V (Fig. S5). The measured current magnitudes were converted into 15 conductance states according to $|G_k| = |I_k|/|V_{ds}|$, yielding values ranging from 0.65 to 2.00 μS. These experimentally derived conductance states were normalized to construct the allowed G15 state set. During the device-constrained simulation, the magnitudes of the classifier weights and biases were mapped to the nearest available G15 state, while their original signs were retained separately, corresponding conceptually to a differential representation of positive and negative parameters. Therefore, Scheme D (R15 + G15) applies the experimentally measured R15 photoresponse-state constraint to the front-end filters and the experimentally derived G15 conductance-state constraint to the classifier. The input images, feature dimensions, classifier architecture, dataset partition, and training conditions were otherwise kept identical to those of the other schemes. This procedure represents device-constrained numerical simulation rather than a physically integrated neural-network implementation.

References

[1] Liu B L, Köpf M, Abbas A N, et al. Black arsenic-phosphorus: Layered anisotropic infrared semiconductors with highly tunable compositions and properties. Adv Mater, 2015, 27(29): 4423-4429.

[2] Mak K F, Lee C, Hone J, et al. Atomically thin MoS_2: A new direct-gap semiconductor. Phys Rev Lett, 2010, 105(13): 136805.

[3] Gong C, Zhang H J, Wang W H, et al. Band alignment of two-dimensional transition metal dichalcogenides: Application in tunnel field effect transistors. Appl Phys Lett, 2013, 103(5): 053513.
[4] Wu F, Li Q, Wang P, et al. High efficiency and fast van der Waals hetero-photodiodes with a unilateral depletion region. Nat Commun, 2019, 10(1): 4663.